Dynamics of time-modulated, nonlinear phononic lattices

B. L. Kim,[1] C. Chong,[2] S. Hajarolasvadi,[3,*] Y. Wang,[4] and C. Daraio[1,†]
[1]*Department of Mechanical and Civil Engineering, California Institute of Technology, Pasadena, California 91125, USA*
[2]*Department of Mathematics, Bowdoin College, Brunswick, Maine 04011, USA*
[3]*Department of Civil and Environmental Engineering, University of Illinois at Urbana-Champaign, Urbana, Illinois 61801, USA*
[4]*School of Mechanical and Aerospace Engineering, Nanyang Technological University, Singapore, Republic of Singapore 6397984*

(Received 1 July 2022; revised 5 January 2023; accepted 14 February 2023; published 23 March 2023)

The propagation of acoustic and elastic waves in time-varying, spatially homogeneous media can exhibit different phenomena when compared to traditional spatially varying, temporally homogeneous media. In the present work, the response of a one-dimensional phononic lattice with time-periodic elastic properties is studied with experimental, numerical and theoretical approaches in both linear and nonlinear regimes. The system consists of repelling magnetic masses with grounding stiffness controlled by electrical coils driven with electrical signals that vary periodically in time. For small-amplitude excitation, in agreement with linear theoretical predictions, wave-number band gaps emerge. The underlying instabilities associated to the wave-number band gaps are investigated with Floquet theory and the resulting parametric amplification is observed in both theory and experiments. In contrast to genuinely linear systems, large-amplitude responses are stabilized via the nonlinear nature of the magnetic interactions of the system, and results in a family of nonlinear time-periodic states. The bifurcation structure of the periodic states is studied. It is found the linear theory correctly predicts parameter values from which the time-periodic states bifurcate from the zero state. In the presence of an external drive, the parametric amplification induced by the wave-number band gap can lead to bounded and stable responses that are temporally quasiperiodic. Controlling the propagation of acoustic and elastic waves by balancing nonlinearity and external modulation offers a new dimension in the realization of advanced signal processing and telecommunication devices. For example, it could enable time-varying, cross-frequency operation, mode- and frequency-conversion, and signal-to-noise ratio enhancements.

DOI: 10.1103/PhysRevE.107.034211

I. INTRODUCTION

Acoustic metamaterials and phononic crystals often achieve control of wave propagation by leveraging scattering effects induced by the presence of spatial periodicity in the design of their microstructure [1–5]. In active mechanical systems, the periodic variation of material properties in time provides an additional, less-explored strategy to control acoustic and elastic waves. This strategy draws inspiration from the study of parametric amplifiers [6,7] and the effects of traveling-wave-like harmonic modulations (i.e., periodic in both space and time) on electromagnetic waves [8,9]. Indeed, spatiotemporally periodic acoustic and elastic systems have been shown, both theoretically and experimentally, to exhibit the characteristic opening of band gaps in their dispersion relations. Most studies have focused on the presence of nonreciprocal frequency band gaps in linear systems, such as beams and metamaterials with spatially and temporally varying resonators or continuous elastic structures with spatiotemporally periodic properties [10–20].

Whereas frequency band gaps are the hallmark of spatially periodic systems, gaps in the wave-number axis of a linear medium's dispersion relation have been shown to arise in time-periodic and spatiotemporally periodic systems, in which the wave speed of the traveling-wave-like-modulation is greater than the velocity of propagation of the medium [9,15,21–25]. These so-called wave-number band gaps are understood to be parametrically amplified standing waves (i.e., nonpropagating, hence the analogous notion of a band gap) [6,21,23]. For example, in a phononic lattice with a supersonic traveling-wave modulation, incident signals within the induced wave-number band gap excite unstable oscillations of the scattered field. This results in apparent amplification of frequencies corresponding to the band gaps, which are different for forward- and backward-propagating waves since this form of spatiotemporal modulation breaks reciprocity [15]. In another example, an elastic waveguide is modulated periodically only in time via an array of piezoelectric patches controlling the stiffness. The reflection of a broadband signal incident on the interface of the modulated region is observed to comprise narrowband content at half the modulation frequency, consistent with the parametrically amplified standing wave solution present within wave-number band gaps [23]. Generally, in a lossy mechanical medium, the gain realized by time-periodic modulation may compensate for or balance energy dissipation [26]. Wave-number band gaps have been shown to open experimentally in transmission lines and theoretically in proposed photonic systems [21,24]. In a system

*Also at Department of Mechanical and Civil Engineering, California Institute of Technology.
†daraio@caltech.edu

more analogous to the present study, instabilities in a linear phononic lattice with time-modulated, spatially periodic modulations have been explored [27], but the opening of wave-number band gaps in the dispersion relation of phononic systems has not been directly shown.

Aside from periodicity, the introduction of nonlinearity provides an alternative strategy to control waves in discrete chains. The role of nonlinearity in discrete chains, for example, has been studied extensively since the first analysis of the Fermi-Pasta-Ulam-Tsingou problem [28,29]. Some examples include nonlinearity-induced band gaps [30–32], nonreciprocal transmission [33], discrete breathers [34–36], solitary waves [37–39] frequency conversion [40], and nonlinear dispersion [41–44]. A more comprehensive review of the extensive work done on nonlinear lattices can be found in the review articles [45–47] or books [48–51].

Nonlinear effects and their interplay with parametric amplification have indeed been studied in photonic and transmission line systems, which serve as practically implementable analogs to one-dimensional optical metamaterials. Multistability has been shown in Kerr nonlinear photonic crystals [52–54] as well as transmission lines with nonlinear capacitance [55]. Parametric amplification in nonlinear transmission lines has also been demonstrated [56,57]. Unidirectional soliton-like edge states in nonlinear Floquet topological insulators, which are modeled by a discrete nonlinear Schrödinger equation with time variable coefficients, were explored in [58]. The interactions between extrinsic time-periodic modulation and nonlinear effects in phononic systems, however, have typically only been investigated in the limits of linearized behavior of nonlinear systems [59].

In the present study, we investigate a time-modulated phononic lattice in both linear and nonlinear regimes using a combination of experiments, theory and numerical simulations. In addition to the experimental observation of wave-number band gaps, we demonstrate how the linear dynamics can partially explain the observed bifurcation structure of time-periodic states that result due to the presence of nonlinearity. The linearized theory is complemented by a detailed nonlinear bifurcation analysis that exploits a fixed point algorithm for the computation of time-periodic orbits and a pseudo-arclength continuation. This bifurcation structure provides a road map to understand hysteretic behavior observed in the system in the presence of an external drive, where both time-periodic and temporally quasiperiodic states are found to coexist.

The paper is structured as follows: The experimental platform and corresponding model equations are detailed in Secs. II and III, respectively. Results on wave-number band gaps and their associated instabilities in the small-amplitude regime and a parametric investigation of stability are reported in Sec. IV. Nonlinear effects leading to the formation of stable temporally time-periodic and quasiperiodic orbits are explored in Sec. V. Section VI concludes the paper.

II. EXPERIMENTAL PLATFORM

The experimental setup is adapted from the platform developed by Wang *et al.* [15]. A one-dimensional (1D) phononic

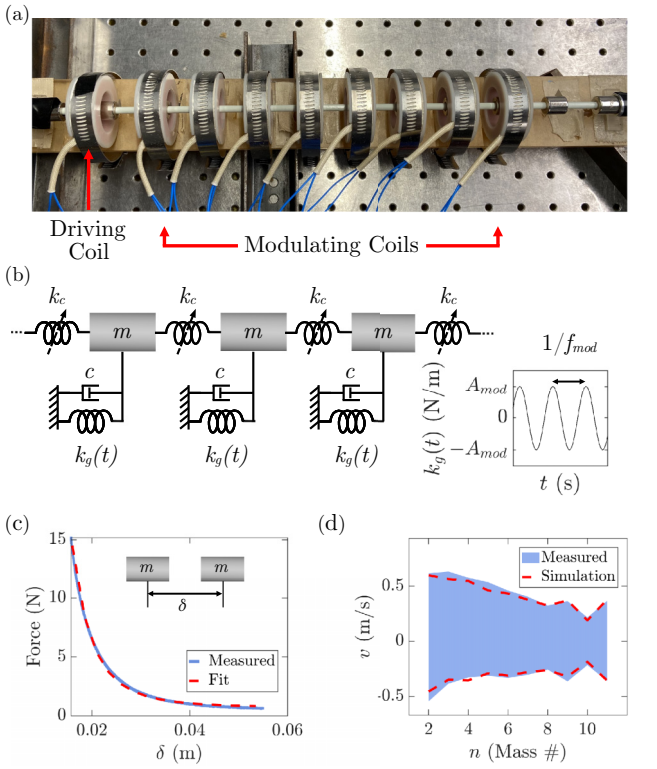

FIG. 1. (a) Photo of the experimental apparatus, with electromagnetic coils corresponding to grounding springs (modulating coils) and ring magnets inside each coil (not fully visible) sliding freely on a low-friction rod. (b) Schematic of the mass-spring lattice model with nonlinear coupling stiffness k_c, time-varying grounding stiffness $k_g(t)$, and viscous damping c; right panel shows the harmonic modulation form of the time-varying grounding stiffness. (c) Force-distance measurement (blue line) [15] and fit (red dashed line) of repulsive magnetic force between neighboring masses (d) Measured (blue shaded region) and numerically simulated (red dashed lines) nodal velocity envelope, used for viscous damping parameter fitting by matching spatial decay.

lattice is realized as a mass-spring chain composed of N ring magnets (K&J Magnetic, P/N R848) lined with sleeve bearings (McMaster-Carr P/N 6377K2) comprising the uniform masses, arranged with alternating polarity on a smooth rod (McMaster-Carr, P/N 8543K28). Electromagnetic coils (APW Company SKU, FC-6489) are fixed concentrically around the equilibrium positions of each of the innermost eight masses, such that they may exert a restoring force on each mass proportional to an applied current. The chain has fixed boundary conditions, and the input mass (the first free inward mass from one of the fixed ends) has a concentric electromagnetic coil offset axially from its equilibrium position, which provides the driving force. Figure 1(a) shows the experimental setup. A lattice of size $N = 12$ (with fixed boundaries $n = 1$ and $n = 12$) is selected, to cover a sufficient range of wavelengths for the investigation of transmission and dispersion of waves, while minimizing the role of frictional losses.

The modulated magnetic lattice is modeled as a monatomic, nonlinear mass-spring chain with dynamically variable grounding springs and linear damping [see Fig. 1(b)].

The magnetic repulsive force between adjacent masses provides the nonlinear coupling stiffness, where the experimental force-distance relation is fit as a dipole approximation, as shown in Fig. 1(c). For small displacements, the coupling stiffness may be approximated as a linear spring, taking the slope of the force-distance relation at the equilibrium mass spacing. The modulating electromagnetic coils are modeled as a grounding stiffness applied to each mass, which may be positive or negative. A sinusoidal current applied uniformly (and in phase) to every modulating coil provides time-periodic grounding stiffness modulation $k_g(t)$, shown in Fig. 1(b). Experimentally measured values for the force exerted on each mass by the magnetic field induced by each concentric electrical coil are used in analytical and numerical models (data from [15]). Dissipative forces, modeled as linear dashpots, are estimated with a fitting parameter (see Sec. III).

III. MODEL EQUATIONS

The lattice is modeled as a discrete mass-spring chain, wherein the equation of motion for the nth mass (ring magnet) with displacement u_n may be written as [15]

$$m\frac{d^2u_n}{dt^2} + k_g(t)u_n + F_{\text{loss},n} + F_{\text{mag},n} = \delta_{2,n}A_{dr}\cos(2\pi f_{dr}t), \tag{1}$$

for $n = 1$ to N, with fixed boundary conditions $u_1(t) = u_N(t) = 0$. All ring magnets have uniform mass m. The dissipative forces are represented by $F_{\text{loss},n}$, and $F_{\text{mag},n}$ is the coupling force acting on the nth mass due to repulsive force between neighboring ring magnets. The driving input amplitude and frequency are given by $A_{dr}([A_{dr}] = \text{N})$ and $f_{dr}([f_{dr}] = \text{Hz})$, respectively. The Kronecker delta, $\delta_{2,n}$, acts so that the input forcing applies only to mass $n = 2$.

An AC sinusoidal voltage (with zero DC offset) applied to the electromagnetic coils induces a harmonic grounding stiffness modulation of the form

$$k_g(t) = \delta_{j,n}A_{\text{mod}}\cos(2\pi f_{\text{mod}}t) \tag{2}$$

with amplitude A_{mod} ($[A_{\text{mod}}] = \text{N m}^{-1}$) and frequency f_{mod} ($[f_{\text{mod}}] = \text{Hz}$) [see Fig. 1(b) inset]. The Kronecker delta index $j = 3$ to $N-2$ so that the modulation acts only on masses $n = 3$ to $N-2$, labeled as in Fig. 1(a). The amplitudes A_{dr} and A_{mod} are determined using empirical relations between applied voltage and resultant current in the coils and measurements of the reaction force exerted by the coils on the concentric ring magnets as a function of displacement from equilibrium position for a given current [15]. The stiffness (in N m^{-1}) of each coil is approximately $A_{\text{mod}} \approx 81A_V$ for applied voltages $A_V < 0.575$ V, and $A_{\text{mod}} \approx 39 + 14A_V$ for voltages $A_V \geqslant 0.575$ V. The driving is offset from the equilibrium position of the driven mass by 7.5 mm, therefore the driving amplitude A_{dr} (in N) is obtained by multiplying the previous stiffness-voltage relations by the offset.

Dissipative forces are modeled phenomenologically with a viscous damping term,

$$F_{\text{loss},n} = c\frac{du_n}{dt}, \tag{3}$$

where the damping coefficient c ($[c] = \text{N s m}^{-1}$) is determined empirically. Because strong dissipation causes rapid decay of free oscillations in time (on the order of one period), it is better for this system to estimate the damping constant by considering spatial decay. We measure and simulate monochromatic waves excited from the driving coil traveling through the lattice for multiple frequencies spanning the pass band of the lattice. We then minimize the difference (in the least squares sense) between the simulated and experimental velocity-amplitude envelopes as a function of the damping constant. A representative example of the matched measured and simulated velocity envelopes is shown in Fig. 1(d). The value of c that minimized the magnitude of the difference is used in all analytical and numerical modeling.

The coupling force term is defined using the repulsive magnetic force $P(x)$ between neighboring masses, where $P(x)$ is a function of the center-to-center distance x (m) between masses. The measured force-distance relation between neighboring masses is fit with a dipole-dipole approximation given by

$$P_{\text{dipole}}(x) = k_{\text{dipole}}x^{-\alpha} + P_{0,\text{dipole}}. \tag{4}$$

The measured and dipole-dipole fit values are shown in Fig. 1(c). If the displacement amplitude of the masses is small relative to the equilibrium distance between adjacent masses, it is useful to employ a linear approximation using the Taylor expansion of the above expression about the equilibrium displacement

$$P_{\text{linear}}(x) = k_{\text{linear}}x, \tag{5}$$

where $k_{\text{linear}} = P'_{\text{dipole}}(a)$, where a is the equilibrium distance between adjacent masses. Thus, the total coupling force on a given mass is calculated using its displacement u_n and the displacement of the neighboring masses $u_{n\pm1}$ as follows:

$$F_{\text{mag},n} = P(a - u_n + u_{n+1}) - P(a - u_{n-1} + u_n), \tag{6}$$

where P can be given by either P_{dipole} or P_{linear}.

Table I summarizes the measured and fit parameters used throughout the paper. For all simulations, we use a variable step fourth-order Runge-Kutta method as implemented in MATLAB ode45. This has been shown to be accurate in other related nonlinear lattice problems [50].

TABLE I. Lattice model parameters.

Measured		Fit	
Parameter	Value	Parameter	Value
m	0.0097 kg	c	0.15 N s m^{-1}
a	33.4 mm	k_{linear}	87.03 N m^{-1}
$f_{\text{mod}} = \omega_{\text{mod}}/(2\pi)$	$\in$ [1 70] Hz	k_{dipole}	9.044×10^{-7} N m^4
$f_{dr} = \omega_{dr}/(2\pi)$	$\in$ [1 40] Hz	$P_{0,\text{dipole}}$	0.7047 N
		A_{mod}	$\in$ [0 100] N m^{-1}
		A_{dr}	$\in$ [0.15 0.4] N

IV. WAVE-NUMBER BAND GAPS

A. Theoretical determination of wave-number band gaps

In the small-amplitude displacement regime, we observe experimentally the existence of wave-number band gaps. In this section, we summarize the linear theory predicting parameter values that lead to the emergence of wave-number band gaps in our system. In the limit of small displacements, we employ the linear approximation of the magnetic intersite coupling discussed previously. Ignoring damping (which we return to later) and assuming that the chain is infinite in length results in the following model

$$m\frac{d^2u_n}{dt^2} + A_{\text{mod}}\cos(2\pi f_{\text{mod}}t)u_n + k_{\text{linear}}(2u_n - u_{n-1} - u_{n+1}) = 0. \tag{7}$$

One approximate solution of this equation will be the sum of the incident wave and the scattered fields induced by the time modulation [12],

$$u_n(t) = U_{-1}e^{i(q_0n-2\pi f_{-1}t)} + U_0e^{i(q_0n-2\pi f_0t)} + U_1e^{i(q_0n-2\pi f_1t)}, \tag{8}$$

where f_0 is the ordinary frequency of the incident wave with amplitude U_0 and $q_0 = \kappa_0 a$ is the dimensionless form of the wave number. Note, an analysis that includes all harmonics is discussed in Sec. IV C. The amplitudes of the scattered fields are U_{-1} and U_1, which have frequencies $f_{\pm1} = f_0 \pm f_{\text{mod}}$. The coupling between the incident and scattered fields is negligible except where $D(f_0, q_0) = D(f_{\pm1}, q_0) = 0$ [12,15], where

$$D(f, q) := m(2\pi f)^2 - 4k_{\text{linear}}\sin^2(q/2) = 0 \tag{9}$$

is the usual dispersion relationship in the unmodulated lattice (i.e., $A_{\text{mod}} = 0$). The intersections occur precisely when $f_0(q) = f_{\text{mod}}/2$. Substituting Eq. (8) into Eq. (7) and equating coefficients of the three harmonics leads to a zero determinant condition [12], and is given by the expression

$$\hat{D}(f, q) = D(f - f_{\text{mod}}, q)D(f, q)D(f + f_{\text{mod}}, q) - A_{\text{mod}}^2[D(f - f_{\text{mod}}, q) - D(f + f_{\text{mod}}, q)] = 0. \tag{10}$$

This condition is a modified dispersion relation in the neighborhood of the intersections of $D(f_{\pm1}, q_0) = 0$ and $D(f_0, q_0) = 0$. Values of q that lead to solutions of Eq. (10) with complex valued f makeup the so-called wave-number band gaps in the band structure and correspond to a parametrically amplified standing wave with growth rate given by the imaginary part of f [23,24]. The analytical dispersion relations for the unmodulated ($D(f, q) = 0$) and modulated ($\hat{D}(f, q) = 0$) lattices are shown in Figs. 2(a) and 2(b), respectively, for parameters $f_{\text{mod}} = 40$ Hz and $A_{\text{mod}} = 37.5$ N m^{-1}. As predicted by the intersection of the incident and scattered fields, the wave-number band gap opens at $f = f_{\text{mod}}/2$, as seen in Fig. 2(c).

To verify the dispersion calculations, we simulate Eq. (1) using the same modulation parameters for the grounding stiffness $k_g(t)$ and mass m that were used to compute the dispersion relationships, but we use the nonlinear repulsive force (P_{dipole} instead of P_{linear}), and we include viscous damping c (see Table I for the specific values used). The simulation is solved repeatedly for monochromatic, six-cycle sine bursts from $f_{dr} = 1$ to 40 Hz (in 1 Hz increments) with driving amplitude $A_{dr} = 0.38$ N. The numerical dispersion relationship is obtained by computing the two-dimensional Fourier

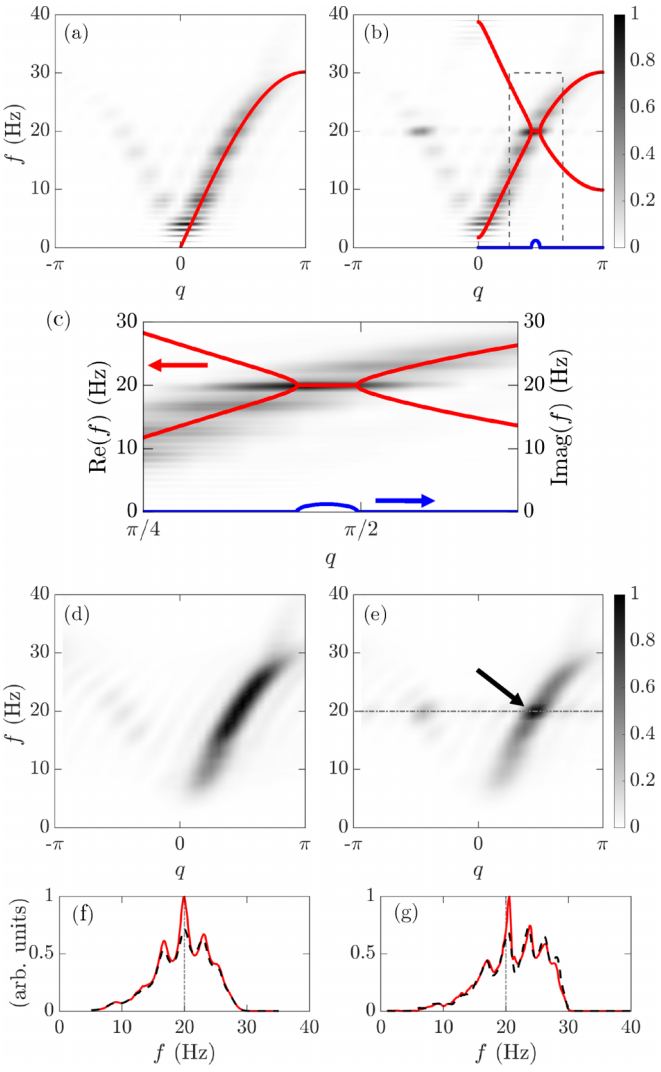

FIG. 2. Dispersion relation and transmission response in unmodulated and modulated lattice at $f_{\text{mod}} = 40$ Hz. (a) Numerical dispersion reconstruction for the unmodulated lattice. The analytical predication is shown by the red curve. (b) Numerical dispersion reconstruction with modulation frequency $f_{\text{mod}} = 40$ Hz. The real part (red curve) and imaginary part (blue curve) of the analytical approximation is also shown. (c) Expanded view of the band gap from the gray dashed window in panel (b). (d) Experimentally measured dispersion reconstruction for the unmodulated lattice. (e) Experimentally measured dispersion reconstruction with modulation frequency $f_{\text{mod}} = 40$ Hz. The frequency $f_{\text{mod}}/2 = 20$ Hz is indicated by the gray dash-dotted line. The arrow highlights amplitude peak in dispersion branch. (f) Numerically simulated frequency transmission spectra for the unmodulated lattice (black dashed curve) and modulated lattice (red curve) with $f_{\text{mod}} = 40$ Hz. The frequency $f_{\text{mod}}/2 = 20$ Hz is indicated by the gray dash-dotted line. (g) Same as panel (f), but for the experimentally measured frequency transmission spectra.

transform (2DFFT) of the velocity components of the numerical solutions. Color intensity corresponds to the normalized spectral energy density (a composite of all driving frequencies) of the unmodulated ($A_{\text{mod}} = 0$ N m^{-1}) and modulated ($A_{\text{mod}} = 37.5$ N m^{-1}) lattices in Figs. 2(a) and 2(b), respectively. This method is similar to a spectral energy density method frequently employed in photonic and phononic systems [12,15,60]. The numerical dispersion relation accounts for nonlinearity, gain, losses, and finite effects but still agrees well with the linear theory based on the infinite losses lattice with only three fields used to determine the dispersion relationship.

B. Experimental observation of wave-number band gaps

To reconstruct the dispersion relation of acoustic waves propagating through the experimental lattice, we measure the velocity of each mass using a laser Doppler vibrometer (LDV, Polytec CLV-2534). We use these measurements to construct a full space-time-resolved transient velocity response of the lattice. The leftmost free mass $n = 2$ is driven by a monochromatic, six-cycle sine wave burst from quiescent initial conditions, exciting a right (forward) traveling wave. The finite-cycle burst and termination time of each measurement are chosen so that reflections off the right boundary $n = 12$ are not captured. Using the velocity field measurements from driving frequencies from from $f_{dr} = 1$ to 35 Hz (in 1 Hz increments), a composite of spectral energy densities of the two-dimensional velocity fields yields a reconstruction of the dispersion relation (the same method used in the numerical simulations). Figures 2(a), 2(b), 2(d), and 2(e) show the comparison of measured dispersion against the numerical simulation overlaid with the analytical predictions.

The measured dispersion reconstruction in Fig. 2(d) for the lattice without external modulation exhibits the expected behavior of a monatomic lattice, i.e., a single acoustic branch terminating at the edge of the Brillouin zone. The positive wave-number branch corresponds to forward (right) traveling waves, while the negligible intensity negative wave-number branch indicates the absence of backward (left) traveling waves in the unmodulated lattice.

The measurements are then repeated with an extrinsic temporal grounding stiffness modulation applied to the lattice via the electromagnetic coils. The effective grounding stiffness of the masses are modulated harmonically at $f_{\text{mod}} = 40$ Hz. Dissipation in the experimental apparatus makes detection of small wave-number signals difficult; therefore, the modulation frequency is selected so that the salient features of the wave-number band gap, which occur at $f_{\text{mod}}/2$, lie on a clear section of the dispersion branch. The numerical and experimental dispersion reconstructions shown in Figs. 2(b) and 2(e), respectively, exhibit a strong peak (i.e., darker regions in the spectral energy density), at $f_{\text{mod}}/2 = 20$ Hz on the dispersion branch. In the numerical simulation, this peak aligns with the analytical prediction of the wave-number band gap, and the experimental peak is highlighted by an arrow and seen to align with $f_{\text{mod}}/2 = 20$ Hz. This increased amplitude response is consistent with the expected parametric amplification, associated with the complex frequency inside the wave-number band gap, and is in line with previous results in the literature [23,24]. Compared to the unmodulated lattice, the dispersion branch of the modulated lattice is largely unchanged, except for the small neighborhood of frequencies around $f_{\text{mod}}/2 = 20$ Hz.

Both the experimental and numerical results show good agreement in the presence of time modulation, and the location of the wave-number band gap is predicted accurately by the analytical model. Moreover, an additional amplitude peak is observed at $f_{\text{mod}}/2$ and the negative of the wave number corresponding to the band gap, where the negative wave number may be interpreted as backward propagating waves [Figs. 2(b) and 2(d)]. Such behavior is consistent both with the predicted parametrically amplified standing wave solution that occurs within the wave-number band gap and with previous experimental work that has shown evidence of the same effect via the conversion of broadband signals into narrowband reflections [23].

In addition to exploring dispersion of traveling waves, we examine the transmission spectrum of the harmonically driven lattice. The lattice is driven harmonically at the input mass $n = 2$ by the reference signal of a lock-in amplifier (LIA, Stanford Research SR860). The reference signal is a continuous sine sweep from $f_{dr} = 1$ to 40 Hz, which is sufficiently slow for the lattice to exhibit effectively steady-state behavior. The output velocity at mass $n = 11$ is measured using the LDV, and the output is multiplied by the reference signal and integrated over a moving time window by the LIA. This gives a spectrum of the amplitude of the lattice response versus frequency, relative to the constant input amplitude of the LIA reference signal. Experimental parameters are identical to the dispersion reconstruction, with $f_{\text{mod}} = 40$ Hz, $A_{\text{mod}} = 37.5$ N m^{-1}, and $A_{dr} = 0.38$ N. This is also reproduced in numerical simulation. The resulting frequency spectrum demonstrates clearly that the extrinsic time-periodic modulation induces amplification of signals at half the modulation frequency, in both experiment and simulation; see Figs. 2(f) and 2(g), respectively. The relatively narrowband amplification provides further evidence that the dispersion reconstruction accurately depicts the localized nature of the wave-number band gap and its amplifying effect on incident signals.

C. Parametric investigation of stability

A more complete analysis of stability can be achieved by considering more than the three modes included in Eq. (8) that result in a complex-valued f. Moreover, the inclusion of damping also has a nontrivial effect on the stability properties. Therefore, we conduct a stability analysis on the linearized equations of motion of an infinite mass-spring chain with damping,

$$m\frac{d^2u_n}{dt^2} + c\frac{du_n}{dt} + A_{\text{mod}}\cos(2\pi f_{\text{mod}}t)u_n + k_{\text{linear}}(2u_n - u_{n-1} - u_{n+1}) = 0. \tag{11}$$

In particular, we make use of a discrete Fourier transform,

$$\hat{u}(q,t) = \sum_{n\in\mathbb{Z}} u_n(t)e^{iqn}, \tag{12}$$

to cast Eq. (11) in Fourier space,

$$\partial_t^2 \hat{u}(q,t) + \frac{c}{m}\partial_t \hat{u}(q,t) + \left[(2\pi f(q))^2 + \frac{A_{\text{mod}}}{m}\cos(2\pi f_{\text{mod}} t)\right]\hat{u}(q,t) = 0, \tag{13}$$

where $D(f(q), q) = 0$, that is $f(q)$ satisfies the dispersion relation in the unmodulated lattice. Equation (13) is a Mathieu equation, which includes a linear viscous damping term [61–65].

The stability regions of the Mathieu equation can be approximated analytically. The standard form of the Mathieu equation is $\ddot{x}(t) + \gamma\dot{x}(t) + [\delta + \epsilon\cos(t)]x(t) = 0$ where $\gamma = \frac{c}{m2\pi f_{\text{mod}}}$, $\delta = (\frac{f(q)}{f_{\text{mod}}})^2$, and $\epsilon = \frac{A_{\text{mod}}}{(2\pi f_{\text{mod}})^2 m}$. In the absence of damping, regions of instability in the $[\delta, \epsilon]$ parameter plane emerge at the values $\delta_j = \frac{j^2}{4}$, where j is an integer [66]. If one considers the parametric plot $s(q) = [\delta(f(q)), \epsilon(f(q))]$ in the stability diagram of the Mathieu equation, one sees that $s(q)$ must cross the first instability tounge since $f(q)$ is continuous and increases monotonically from zero, assuming an infinite lattice. Thus, a condition for stability in the limit of small modulation amplitude can be obtained by considering the instability tongue associated to $j = 1$, namely, that $(\frac{f(q)}{f_{\text{mod}}})^2 < 1/4$. This recovers the result that instability is induced by the intersection of dispersion curves when $f(q) = f_{\text{mod}}/2$, as discussed in Sec. IV A.

In a finite-sized lattice with zero boundary conditions, the set of wave numbers is discrete and is given by $q_r = \pi r/(N-1)$. Thus, to derive a condition for stability in the finite lattice case, each frequency must be inspected, since it is possible that the parametric set of points given by $s(q_r)$ may never fall in the first instability region due to the discrete nature of q_r in the finite lattice.

We now derive the stability condition in a finite lattice in the presence of damping. The transition curves of the the stability regions of the Mathieu equation with damping and small but finite modulation amplitude can be found via perturbation analysis [64,66],

$$\delta = \frac{1}{4} \pm \frac{\sqrt{\epsilon^2 - \gamma^2}}{2}, \tag{14}$$

which is valid for small ϵ. In terms of the original system parameters f_{mod} and A_{mod}, Eq. (14) implies the following condition for stability, which considers all $N-2$ wave numbers of the finite system given by $q_r = \pi r/(N-1)$,

$$\max_{1\leqslant r\leqslant N-2}\left|\left(\frac{f(q_r)}{f_{\text{mod}}}\right)^2 \pm \frac{1}{2}\sqrt{\left(\frac{A_{\text{mod}}}{(2\pi f_{\text{mod}})^2 m}\right)^2 - \left(\frac{c}{m2\pi f_{\text{mod}}}\right)^2}\right| < \frac{1}{4}. \tag{15}$$

The black line of Fig. 3(a) shows the transition curves of the regions of instability based on the analytical approximation (15).

While the application of the Mathieu equation in Eq. (15) accounts for the finite length and boundary conditions of the experimental lattice, it does not account for the fact that the experimental lattice is only partially modulated. In particular, the first and last free masses are not modulated in order to allow more accurate measurements of their velocities. In this case, one must compute Floquet multipliers to determine stability. If all Floquet multipliers have modulus not exceeding unity, then the solution (the zero solution in this case) is stable. Otherwise it is unstable (at least one Floquet multipler exceeds unity). See Appendix A for details. The results of this analysis are shown in Fig. 3(a), where the gray shaded region indicates modulation parameters that yield an unstable solution. The qualitative structure of the instability region agrees with the analytical prediction of Eq. (15), but the boundary is shifted to higher modulation amplitudes for some frequencies, which is consistent with the fact that fewer masses in the lattice are gaining energy from modulation.

In order to explore the validity of the linear theoretical stability predictions, we study both the numerically simulated and experimentally measured response of the lattice. The existence of unstable, exponentially growing solutions from the linear model implies large-amplitude displacements, and indeed large-amplitude displacements (relative to the equilibrium spacing a) are experimentally observed. To illustrate the difference between the responses, we simulate the response of the lattice both with the linearized and the nonlinear repulsive force (P_{linear} and P_{dipole} respectively) using the measured and fit parameters matching the experimental setup (see Table I). An unstable set of modulation parameters, as predicted by the linear theory [in particular, $f_{\text{mod}} = 41.6$ Hz, $A_{\text{mod}} = 78\ \text{N m}^{-1}$, see black star in Fig. 3(a)], is applied to the lattice with no input drive ($A_{dr} = 0$). The simulation is initiated with quiescent conditions except for an initial velocity at the driving mass ($n = 2$). It is observed that, while the response of the linear simulation grows exponentially, the nonlinear simulation reaches an oscillatory steady state, sustained by the grounding stiffness modulation. This is illustrated by the velocity responses of the output mass ($n = 11$) in Fig. 3(b), with the linear simulation in gray and nonlinear simulation in black. Conversely, for parameter values where the linear theory predicts stability, the responses of both the linear and nonlinear simulations decay with time due to damping. Thus, as a proxy for the theoretical linear instability, we search the full modulation parameter space for any response that does not decay with time, what we will refer to as nondecaying responses, from the nonlinear simulation or experimental lattice.

The modulation parameters that lead to a nondecaying response for the numerical simulation are denoted in Fig. 3(a) by white markers. The region of modulation parameters that lead to a nondecaying response in the numerical simulation with nonlinear interaction included exhibits good quantitative

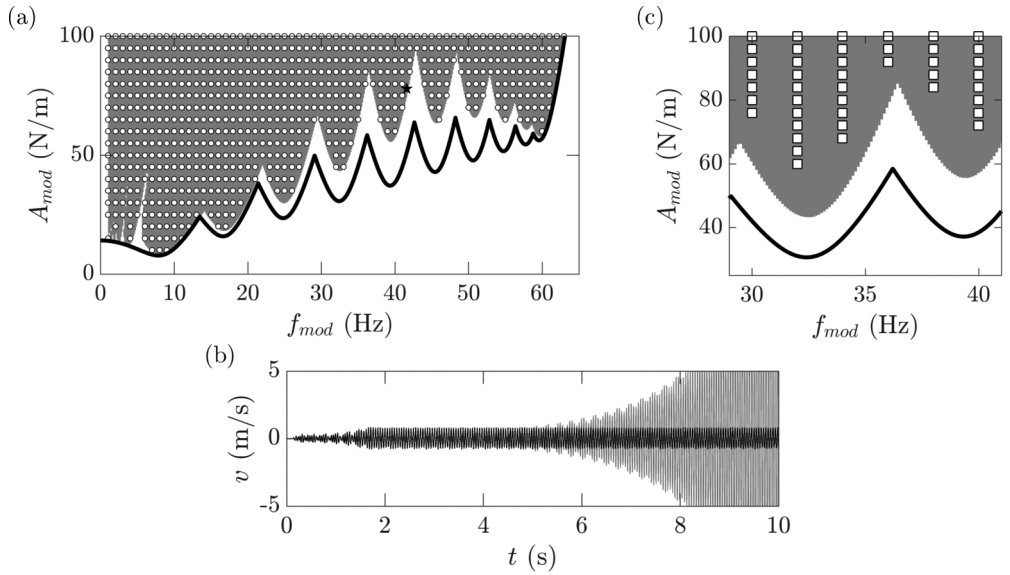

FIG. 3. Stability of modulation parameters. (a) The black curve shows the analytical prediction of the stability boundary based on condition (15). Shaded region indicates unstable solutions for modulation parameter combinations as determined by the Floquet analysis. The white circles indicate parameter combinations for which the fully nonlinear simulation exhibits a nondecaying, modulation-driven response to an initial impulse. The black star indicates the parameters shown in panel (b). (b) Numerically simulated velocity output time series for the parameters indicated by the black star in panel (a). The fully nonlinear simulation (black line) has a bounded response, while the linearized simulation (gray line) exhibits exponential growth. (c) Experimental nondecaying parameter combinations (white squares). The black curve shows the analytical prediction of the stability boundary based on condition Eq. (15). Shaded region indicates unstable solutions for modulation parameter combinations as determined by the Floquet analysis.

agreement with the unstable region predicted through both the Floquet theory and damped Mathieu [Eq. (15)] stability conditions. We perform the same procedure for the experimental setup over a subset of the modulation parameter space, exciting the input mass ($n = 2$) with an impulse and observing decaying or nondecaying responses. The experimental nondecaying region [Fig. 3(c)] shows similarly good agreement with the linear theoretical predictions.

Despite linearization and, in the case of the Mathieu condition, a perturbation method approximate solution, both the Floquet and Mathieu stability conditions accurately predict the ranges of modulation parameters for which a modulation-driven response is observed in the experiment. This suggests that the onset of such modulation-driven response can be predicted, to a degree, by the approximate linear dynamics of the lattice. On the other hand, the nonlinearity is clearly playing an important role in the observed dynamics. As illustrated by Fig. 3(b), the nonlinearity has a stabilizing effect, leading to bounded steady-states rather than unbounded growth as the linear theory predicts. We explore this, and other aspects of nonlinearity, in the next section.

V. NONLINEAR LATTICE DYNAMICS

A. Nonlinear states with no external drive

We now further investigate the interplay of the nonlinearity of the system with the extrinsic time modulation. As a particular case example, we fix the modulation frequency to $f_{\mathrm{mod}} = 41.6$ Hz, which corresponds to the frequency of the star point in Fig. 3(a). At this modulation frequency, the linear theory predicts that the zero state becomes unstable at a modulation amplitude of $A_{\mathrm{mod}} \approx 75.2\ \mathrm{N\,m^{-1}}$ (in the fully modulated lattice the prediction is $A_{\mathrm{mod}} \approx 50.1\ \mathrm{N\,m^{-1}}$). For modulation amplitudes above the threshold, the response initially grows, but eventually settles to a stable, time-periodic state [as suggested by Fig. 3(b)]. The period of oscillation is twice the period of the modulation period, which corresponds to the frequency of the unstable modes lying in the wave-number band gap. In order to better understand these nonlinear time-periodic states, we employ a Newton-type procedure to identify them with high precision. See Appendix A for details on the algorithm. Using a Newton method to find time-periodic solutions allows us to identify solutions that are unstable and to compute bifurcation diagrams, which is not possible through direct dynamic simulations, which can only identify stable solutions. To investigate the dynamical stability of the obtained states, a Floquet analysis is used to compute the Floquet multipliers associated with the solutions. This is done following the procedure detailed in Appendix A. Figure 4 shows example solutions obtained with the Newton method with the parameters $f_{\mathrm{mod}} = 41.6$ Hz and $A_{\mathrm{mod}} = 70\ \mathrm{Nm^{-1}}$. There are two time-periodic solutions found at this parameter set. The panels in the left column correspond to a stable solution and the panels in the right column correspond to an unstable solution. Figure 4(a) shows the profile of the solution at $t = 0$. The inset shows a plot of the Floquet multipliers in the complex plane. All multipliers lie within the unit circle (blue solid line in the inset shown), indicating the solution is stable. Figure 4(c) shows a spatiotemporal intensity plot of the solution over one period of motion, where the oscillating character can been seen. Figure 4(b) shows the profile of the unstable solution, whose instability

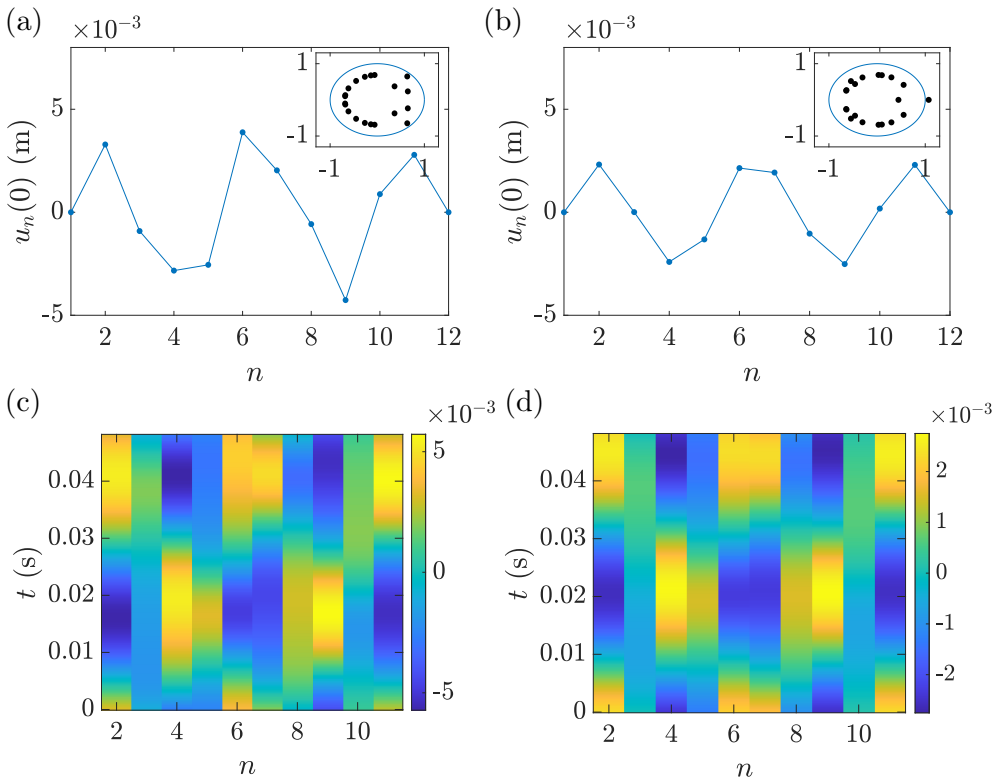

FIG. 4. Time-periodic solutions of Eq. (1) with $f_{\text{mod}} = 41.6$ Hz and $A_{\text{mod}} = 70$ N m^{-1}. (a) Spatial profile of a stable solution. The inset shows the Floquet multipliers. (b) Spatial profile of an unstable stable solution. (c) Intensity plot of the spatiotemporal evolution of the solution shown in panel (a) for one period of motion (color intensity corresponds to displacement). (d) Intensity plot of the spatiotemporal evolution of the solution shown in panel (b).

is indicated by a Floquet multipler lying outside of the unit circle. Figure 4(d) shows the corresponding spatiotemporal intensity plot.

We conduct a bifurcation analysis of the nonlinear time-periodic solutions using a pseudo-arclength continuation [67] with the modulation frequency fixed to $f_{\text{mod}} = 41.6$ Hz and the modulation amplitude A_{mod} as the continuation parameter. The bifurcation diagram is shown in Fig. 5(a). The norm of the initial sate of the solution $\|u(0)\| = \sqrt{\sum_n u_n(0)^2}$ is shown on the vertical axis, and the modulation amplitude is shown on the horizontal axis. Solid blue lines correspond to stable solutions (all Floquet multipliers have modulus not exceeding unity) and red dashed lines correspond to unstable solutions (at least one Floquet multipler exceeds unity). In the diagram, the zero state corresponds to the horizontal line at $\|u(0)\| = 0$ m. The zero state is stable until $A_{\text{mod}} \approx 75.2$ N m^{-1} [the black circle on panel (a) shows the bifurcation point]. This coincides with the prediction based on the linear stability analysis detailed in Sec. IV C. An unstable nonlinear time-periodic state bifurcates from the zero state at the critical modulation amplitude $A_{\text{mod}} \approx 75.2$ N m^{-1}. This unstable nonlinear time-periodic state remains unstable until it undergoes a saddle-node bifurcation at $A_{\text{mod}} \approx 64.44$ N m^{-1} and $\|u(0)\| = .009$ m. The two solutions shown in Fig. 4 correspond to the labels (a) and (b), respectively. This bifurcation implies classic hysteretic behavior is possible. For small modulation amplitudes ($A_{\text{mod}} < 75.2$ N m^{-1}), the zero state will be approached. Once the threshold $A_{\text{mod}} \approx 75.2$ N m^{-1} is exceeded, the zero state is no longer stable, and a small perturbation to the system (like the impulse studied in the previous section) will result in an initial increase in amplitude. However, in the presence of nonlinearity, there exists a stable, time-periodic state, which the dynamics approach asymptotically. For example, with $A_{\text{mod}} = 78$ N m^{-1} [which corresponds to the star in Fig. 3(a)] the zero state is unstable, and thus, the stable time-periodic state is approached upon perturbation, see the star in Fig. 5(a). Once the time-periodic state is excited, one can gradually decrease the modulation amplitude until the saddle-node bifurcation point. Below this point, the dynamics will once again approach the zero state. The bifurcation diagram also implies a region of bi-stability. Namely, the zero state and a time-periodic orbit are stable in the range $64.44 \lessapprox A_{\text{mod}} \lessapprox 75.2$. The bifurcation diagram in the fully modulated lattice is qualitatively similar, but solution curves are shifted; see Appendix B.

B. Nonlinear states in presence of external drive

In the classic paradigm of oscillators with time-independent stiffness, it is well known that presence of damping and external drive can lead to periodic orbits, period-doubling, quasiperiodicity, and chaos [66]. The study of spatially extended lattices (with time-independent stiffness) with damping and external drive is an active research area. Some examples include the study of granular crystals [50,51] and micromechanical oscillator arrays [68]. In such systems,

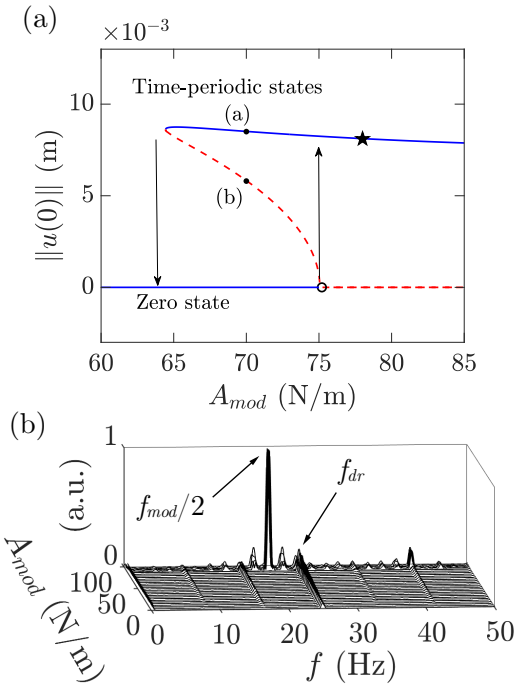

FIG. 5. (a) Bifurcation diagram with $f_{\text{mod}} = 41.6$ Hz fixed showing how time-periodic states bifurcate from the zero state. (b) The frequency response of the experimental lattice for fixed amplitude harmonic driving and increasing harmonic modulation. At a critical amplitude, the lattice transitions from a driving-dominated response to a high-amplitude, modulation-dominated response.

the primary structure is the periodic orbit. Other structures, such as those with higher period, or quasiperiodic ones, typically bifurcate from branches in parameter space consisting of periodic orbits. In this section, we add an external (harmonic) drive to our system with time-dependent stiffness and explore the bifurcations as an underlying parameter is varied. We will demonstrate that the primary structures in the system are quasiperiodic ones, which is in contrast to the periodic ones found in lattices with time-independent stiffness.

When the lattice is driven harmonically, and the modulation amplitude is incrementally increased, we observe a transition from a driving-dominated to a modulation-dominated response, as shown in Fig. 5(b) for the measured steady-state output (mass $n = 11$) velocity. The frequency response shows a sharp transition in dominant frequency component (from driving frequency to half the modulation frequency) and large increase in amplitude. To better understand this, we start by conducting a parametric sweep of the modulation amplitude A_{mod}, both experimentally and numerically. This is a natural parameter to consider for bifurcation studies, since it is expected that larger values of A_{mod} will lead to nonlinear effects. For each value of A_{mod}, the lattice is driven by a harmonic input at one end ($n = 2$), and the output signal is measured at the opposite end ($n = 11$). The velocity response is allowed to reach steady state and the amplitude of the response is recorded. In particular, the magnitude of the temporal Fourier coefficient associated to the drive frequency f_{dr} and half the modulation frequency $f_{\text{mod}}/2$ are recorded. This will indicate if the observed dynamics is due primarily to the drive (i.e., larger Fourier amplitude at $f = f_{dr}$) or the time modulation (i.e., larger Fourier amplitude at $f = f_{\text{mod}}/2$). The modulation amplitude is increased by increment ΔA_{mod}, and the response is again allowed to reach steady state and is recorded. These steps are repeated until the maximum modulation amplitude is reached. We call this procedure the "forward sweep." The "backward sweep" procedure is similar, where A_{mod} is decreased rather than increased. This process is carried out numerically and experimentally. In particular, for the numerical results, Eq. (1) is simulated with the parameters specified in Table I and with drive frequency $f_{dr} = 25$ Hz and drive amplitude $A_{dr} = 0.15$ N. Similar to Sec. V A, we fix the the modulation frequency $f_{\text{mod}} = 41.6$ Hz. Notice that the drive frequency is not a rational multiple of the modulation frequency, which represents a generic choice of these frequencies. The case where one is a rational multiple of the other is briefly discussed in Appendix C. The range of modulation amplitudes considered is $A_{\text{mod}} \in [0, 100]$ N m^{-1} where increments of $\Delta A_{\text{mod}} = 2$ N m^{-1} are used in the sweeps. Experimental forward and backward sweep measurements are repeated four times with identical driving and modulation parameters, with the exception that the step size is $\Delta A_{\text{mod}} \approx 3.75$.

Figure 6 summarizes the results of the modulation amplitude sweeps. In Fig. 6(a) the response of the lattice to a forward sweep of modulation amplitude is analyzed. The relative Fourier amplitudes of the drive frequency $f = f_{dr}$ are shown in blue [squares (line)] and the Fourier amplitudes of the half modulation frequency $f = f_{\text{mod}}/2$ are shown in black [triangles (line)]. Error bars show standard deviation for experimental measurements. For small modulation amplitudes, the response is completely dominated by harmonic driving dynamics, and the amplitude of oscillations at $f_{\text{mod}}/2$ is negligible. Then, at a critical modulation amplitude, the output response transitions sharply from the small displacement, driving signal-dominated regime to a large displacement, modulation-dominated regime, at the sharp jump in the relative amplitude of the $f_{\text{mod}}/2$ (black) in Fig. 6(a). Figure 6(b) examines the transition between the amplitude jumps in more detail. Since only the modulation-dominated response is necessary to track the transition of the lattice between the two states, Fig. 6(b) shows a comparison of the relative Fourier amplitude of $f = f_{\text{mod}}/2$, this time for both the forward (black) and backward sweep (gray) of the modulation amplitude A_{mod} near the transition point. Significant hysteresis is observed in both the experiment (markers) and simulation (dashed lines). This transition occurs at approximately $A_{\text{mod}} = 90$ N m^{-1} in the experiments and $A_{\text{mod}} = 73$ N m^{-1} in simulation for the forward sweep and $A_{\text{mod}} = 60$ N m^{-1} and $A_{\text{mod}} = 63$ N m^{-1} for the measured and simulated backward sweep, respectively.

The structure of the solutions in the low amplitude, drive-dominated region are simple. They are time-periodic with period given by the period of the drive. The solution structure of the higher amplitude, modulation-dominated region is more subtle. To understand this structure, we use Poincaré sections of the output response. A Poincaré section effectively turns a continuous signal into a discrete one by sampling the solution at some fixed time increment, say, T [66]. For

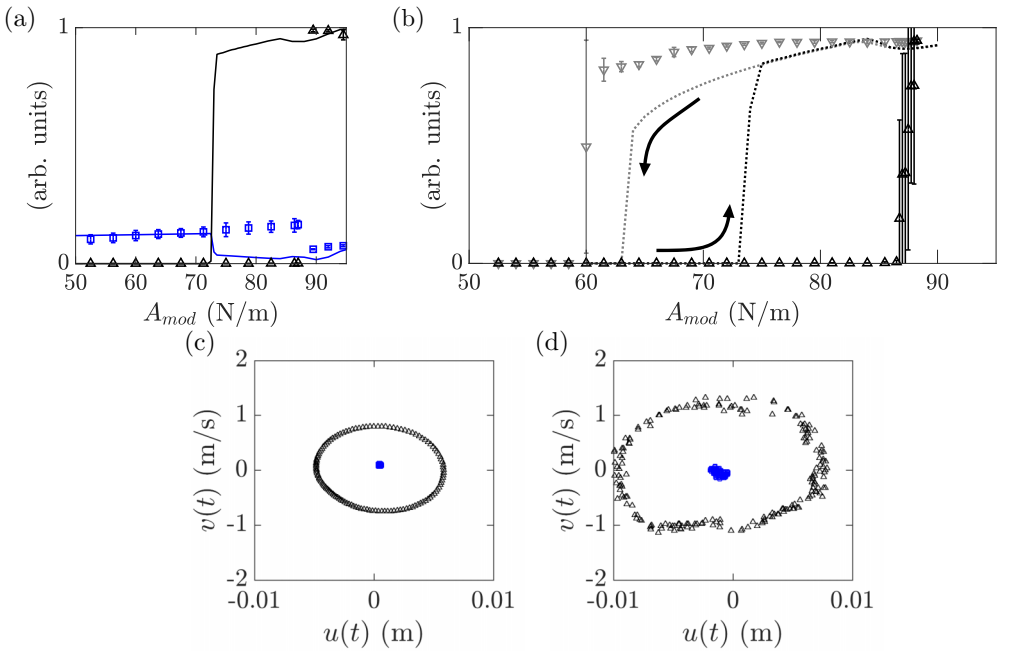

FIG. 6. Nonlinear lattice dynamics (a) Fourier amplitudes for f_{dr} (blue/squares) and $f_{\text{mod}}/2$ [black (triangles)] vs modulation amplitude for experimental (markers) and numerical simulation (lines). Note that error bars are also shown. (b) Hysteresis of $f_{\text{mod}}/2$ Fourier component around mode transition, with slowly increasing (black triangles) and decreasing (gray upside-down triangles) modulation amplitude. Numerical simulation shown in dashed lines. (c) Poincaré section of the output response of the numerical simulation, with sampling period $T = 1/f_{dr}$. Pre- and postforward sweep transition modulation amplitude responses are shown as blue squares and black triangles, respectively. (d) Same as panel (c) for the experiment.

example, a single point in the Poincaré section would correspond to a periodic orbit with period T of the original time series. Two points in the Poincaré section would correspond to a solution with period $2T$ (period doubling), and a closed loop in the Poincaré section would correspond to a quasiperiodic orbit. To create the Poincaré section the output position u (which is found experimentally by integrating the velocity measured by the LDV) and velocity $v = \frac{du}{dt}$ are plotted in the (u, v) phase plane with a sampling period of $T = 1/f_{dr}$. Both numerical simulation and experimental Poincaré sections are sampled at modulation amplitudes at least one ΔA_{mod} smaller and larger than their respective forward sweep transition points. Figure 6(c) shows the numerically simulated Poincaré section at $A_{\text{mod}} = 71$ N m^{-1} (blue squares) and $A_{\text{mod}} = 75$ N m^{-1} (black triangles), and Fig. 6(d) shows the experimentally measured Poincaré section at $A_{\text{mod}} \approx 80$ N m^{-1} (blue squares) and $A_{\text{mod}} = 93$ N m^{-1} (black triangles). Before the transition, the plot of the Poincaré sections reveals a single point, indicating the solution is time-periodic. After the transition, the Poincaré sections form an invariant curve in the phase plane, indicating the solution is temporally quasiperiodic. The Poincaré sections confirm what is already suggested in Fig. 6(a). Namely, there is a single dominant frequency in the response before the transition (time-periodic response) and there are two nonnegligible incommensurate frequencies after the transition (time-quasiperiodic response).

The hysteretic behavior shown in Fig. 6 represents a departure in the hysteretic behavior observed in classic nonlinear systems [66]. Typically the main branch of solutions consist of constant or time-periodic solutions. While quasiperiodic orbits can exist in classic oscillator systems, they are typically unstable (see the discussion in [69]). Here we have demonstrated that in large regions in parameter space, the quasiperiodic orbits are stable. The hysteretic behavior, and the region of bistability, of Fig. 6(b) can be understood in the framework of the previous sections. The reason for this is as follows: In the presence of the external drive, the ground state is no longer the zero state, but rather it is a time-periodic state with frequency identical to the external drive frequency. The quasiperiodic orbit found in the lattice with the external drive results from the combined effect of the nonlinear time-periodic state of the undriven system (discussed in Sec. V A) with frequency $f_{\text{mod}}/2$ and the external drive with frequency f_{dr}. The presence of the two frequencies in the response is what leads to the quasiperiodic motion. With this established, the bifurcation diagram shown in Fig. 5(a) will provide a roadmap for understanding bifurcations in the externally driven system. In particular, the analytical approximation for the jump in the forward sweep is $A_{\text{mod}} \approx 51.1$ N m^{-1}, which is based on the Mathieu equation stability analysis of the fully modulated lattice detailed in Sec. IV C. In the partially modulated lattice (where the first and final node are not modulated), the loss of stability occurs at $A_{\text{mod}} \approx 75.2$ N m^{-1}. This theoretical prediction from the linear analysis is very close to the observed jump shown in Fig. 6(b), $A_{\text{mod}} = 73$ N m^{-1}. Likewise, based on the analysis of Sec. V A the jump in the backward sweep is predicted to occur at $A_{\text{mod}} \approx 64.44$ N m^{-1}, which is close to the observed value of $A_{\text{mod}} \approx 63$ N m^{-1}. Thus, the presence of the external drive did not significantly alter the bifurcation structure [compare Figs. 5(a) and 6(b)]. The underlying solution structure does, however, change significantly. The zero and time-periodic states in the undriven

lattice became time-periodic and quasiperiodic ones in the driven one. The dynamics of a driven lattice with drive frequency that is a rational multiple of the modulation frequency is detailed in Appendix C.

The stability analysis carried out in Sec. IV C can also help explain the observed discrepancy between the experimental results and simulated results (e.g., the region of bistability is slightly larger in the experiment). In Fig. 3(a) one sees that the stability of the lattice with respect to the modulation frequency is very sensitive. In particular, for the modulation frequency $f_{\text{mod}} = 41.6$ Hz used in Fig. 6, the linear stability modulation amplitude (A_{mod}) threshold can change by more than 10 N m^{-1} for a change in f_{mod} of $\pm$ 1 Hz [see boundary of gray instability region in Fig. 3(a)]. Therefore, even a small mistuning between the experimental and theoretical frequency could cause significant changes to the transition modulation amplitude.

While additional tuning of the parameters could yield better quantitative agreement, the primary features of nonlinearity and time modulation are captured well by our model with predetermined parameter values.

VI. SUMMARY AND CONCLUSIONS

We studied the response of a linear and nonlinear discrete, phononic lattice, consisting of magnetic particles controlled by electromagnetic coils. We excited the lattice at one end and imparted external stiffness modulation at each particle site. In the linear regime, we experimentally reconstructed the dispersion relation of a chain with modulated grounding stiffness, demonstrating the opening of wave-number band gaps. For larger modulation amplitudes, the nonlinearity of the coupling force between masses admits bounded solutions that would otherwise not be present in a linear system, where the parametric amplification characteristic of this form of extrinsic modulation induces exponential growth. In particular, the nonlinearity of the system allows for the existence of a family of time-periodic states which bifurcate from the zero state when it losses stability. The combination of external drive and time-modulation allows for the creation of stable, large-amplitude time-quasiperiodic solutions that can coexist with stable, small-amplitude time-periodic ones. This was confirmed both numerically and experimentally, with the experiments showing good qualitative agreement with the numerics.

Our analysis offers validation of the linear dynamics that produce the unique emergent dispersive properties of time-modulated systems, while demonstrating how nonlinearity provides additional flexibility in the design and study of wave propagation time-modulated systems. The findings offer insights on methods to control the propagation of acoustic waves in nonlinear, active systems. Implementing such solutions in small scale devices holds promise for applications in sensing and signal processing, offering frequency agile solutions for tunable filters, delay lines and signal conversion. Such nonlinear phenomena could also be used to compensate losses and dissipation, thereby allowing the miniaturization of components and the addition of on-chip functionalities.

ACKNOWLEDGMENTS

This material is based upon work supported by the U.S. National Science Foundation under Grants No. DGE-1745301 (B.L.K.), No. EFRI-1741565 (C.D.), and No. DMS-2107945 (C.C.). We thank Prof. Bumki Min and Dr. Jagang Park for helpful discussions.

APPENDIX A: CALCULATION OF PERIODIC ORBITS AND FLOQUET MULTIPLIERS

1. Floquet multiplers corresponding to zero state

The stability analysis of the zero state in Sec. IV C is based on a Fourier decomposition in space, which is only valid assuming each node is modulated. If the lattice is partially modulated (like in the experiment, where the first and last nodes are not modulated) one must determine stability based on the numerical computation the Floquet multipliers.

To numerically compute the Floquet multiplers, we solve the full system of equations given by Eq. (1) for the linear case when $F_{\text{mag},n} = k_{\text{linear}}(2u_n - u_{n-1} - u_{n+1})$. The second order system is be reduced to a first-order system $\mathbf{u}'(\mathbf{t}) = \mathbf{A}(t)\mathbf{u}(t)$, where the vector $\mathbf{u}(t)$ contains the displacements and velocities of each mass, and the coefficient matrix $\mathbf{A}(t)$ contains the stiffness, damping, and modulation of the lattice,

$$\mathbf{u}(t) = \begin{pmatrix} u_1(t) \\ \vdots \\ u_N(t) \\ u_1'(t) \\ \vdots \\ u_N'(t) \end{pmatrix}$$

$$\mathbf{A}(t) = \begin{pmatrix} \mathbf{0} & \mathbf{I} \\ -\mathbf{M}^{-1}(\mathbf{K} + \mathbf{K_g}(t)) & -\mathbf{M}^{-1}\mathbf{C} \end{pmatrix}$$

with mass matrix $\mathbf{M} = m\mathbf{I}$, damping matrix $\mathbf{C} = c\mathbf{I}$, stiffness matrix

$$\mathbf{K} = k_{\text{linear}} \begin{pmatrix} 2 & -1 & 0 & \cdots & 0 \\ -1 & \ddots & \ddots & \ddots & \vdots \\ 0 & \ddots & & & 0 \\ \vdots & \ddots & & & -1 \\ 0 & \cdots & 0 & -1 & 2 \end{pmatrix}$$

and modulation matrix

$$\mathbf{K}_g(t) = \begin{pmatrix} 0 & 0 & \cdots & & 0 \\ 0 & k_g(t) & \ddots & & \vdots \\ \vdots & \ddots & \ddots & & \\ & & & k_g(t) & 0 \\ 0 & \cdots & & 0 & 0 \end{pmatrix}.$$

Since the harmonic modulation $k_g(t) = A_{\text{mod}} \cos(2\pi f_{\text{mod}})$ makes the time-dependent coefficient matrix periodic with period $T = 1/f_{\text{mod}}$, we apply Floquet theory to determine the stability the linearized system. At each point $(f_{\text{mod}}, A_{\text{mod}})$ in the modulation parameter space, we solve numerically for the fundamental solution matrix $\mathbf{U}(t)$ at time $t = T$ from initial conditions $\mathbf{U}(t = 0) = \mathbf{I}$. The state is stable if the eigenvalues of $\mathbf{U}(T)$, the Floquet multipliers, have moduli less than one.

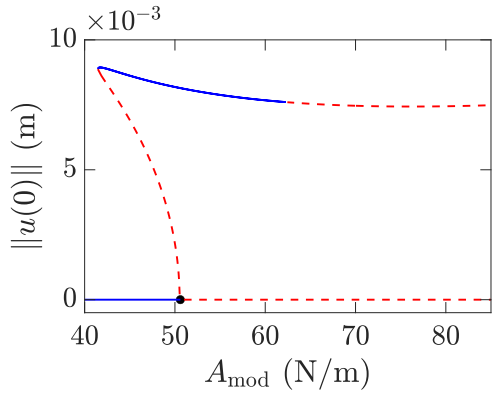

FIG. 7. Bifurcation diagram with $f_{\mathrm{mod}} = 41.6$ Hz fixed showing how time-periodic states bifurcate from the zero state in the fully modulated lattice.

This corresponds to all multipliers lying within the unit circle in the complex plane. Otherwise, the state is unstable. Similar studies have shown this type of Floquet analysis to be an effective method for characterizing instability of propagating waves in discrete systems [25].

2. Newton's method for periodic orbits

Time-periodic orbits are computed by finding roots of the map $F := \mathbf{u}(2T_{\mathrm{mod}}) - \mathbf{u}(0)$, where $2T_{\mathrm{mod}}$ is the period of oscillation and $\mathbf{u}(2T_{\mathrm{mod}})$ is the solution of Eq. (1) at time $2T_{\mathrm{mod}}$ with initial condition $\mathbf{u}(0)$. Roots of this map [and hence time-periodic solutions of Eq. (1)] are found via Newton iterations. This requires the Jacobian of F, which is of the form $V(2T_{\mathrm{mod}}) - I$, where I is the identity matrix, V is the solution to the N^2 variational equations $\dot{V} = DF \cdot V$ where DF is the Jacobian of the equations of motion evaluated at the given state vector. The stability is computed in the same way as detailed above for the zero state, but with the coefficient matrix given by $A(t)$ being replaced by the Jacobian matrix DF.

APPENDIX B: BIFURCATION DIAGRAM IN FULLY MODULATED LATTICE

The bifurcation structure of the time-periodic states in fully modulated lattice with no external drive (see Fig. 7) is similar to the partially modulated lattice, shown in Fig. 5(a).

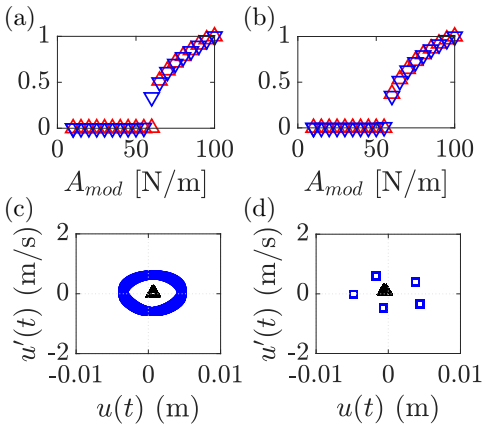

FIG. 8. (a), (b) Forward and backward sweep for driving and modulation frequency combinations that are not (a) and are (b) rational multiples. (c), (d) Poincaré sections for low (black triangles) and high (blue squares) amplitude regime with same frequency combinations as (a) and (b), respectively.

The black circle in the figure indicates when the zero state becomes unstable, according to Eq. (15). This point coincides with the numerically computed time-periodic state bifurcating from the zero state.

APPENDIX C: DRIVING AND MODULATION FREQUENCIES WHICH DIFFER BY A RATIONAL FACTOR

We show a forward and backward sweep of the modulation amplitude for two cases, first, where the driving frequency is a not rational multiple of the modulation frequency ($f_{dr} = 25.77$ Hz, $f_{\mathrm{mod}} = 40$ Hz), and, second, where the driving frequency is a rational multiple of the modulation frequency ($f_{dr} = 25$ Hz, $f_{\mathrm{mod}} = 40$ Hz). It is observed that this does not have a significant impact on the hysteresis behavior, as shown in Figs. 8(a) and 8(b) for the not rational and rational case, respectively. The primary difference is observed in the Poincaré sections for the same frequencies [where Figs. 8(c) and 8(d) are correspond to the same frequencies as Figs. 8(a) and 8(b), respectively]. The outputs for low (black triangles) and high-amplitude (blue squares) modulation regimes, exhibit a quasiperiodic orbit when the frequencies are not rational multiples, while the rational multiple case is periodic.

[1] R. Martínez-Sala, J. Sancho, J. V. Sánchez, V. Gómez, J. Llinares, and F. Meseguer, Sound attenuation by sculpture, Nature (London) **378**, 241 (1995).
[2] R. James, S. M. Woodley, C. M. Dyer, and V. F. Humphrey, Sonic bands, bandgaps, and defect states in layered structures—Theory and experiment, J. Acoust. Soc. Am. **97**, 2041 (1995).
[3] M. S. Kushwaha, P. Halevi, L. Dobrzynski, and B. Djafari-Rouhani, Acoustic Band Structure of Periodic Elastic Composites, Phys. Rev. Lett. **71**, 2022 (1993).
[4] J. O. Vasseur, P. A. Deymier, B. Chenni, B. Djafari-Rouhani, L. Dobrzynski, and D. Prevost, Experimental and Theoretical Evidence for the Existence of Absolute Acoustic Band Gaps in Two-Dimensional Solid Phononic Crystals, Phys. Rev. Lett. **86**, 3012 (2001).
[5] M.-H. Lu, L. Feng, and Y.-F. Chen, Phononic crystals and acoustic metamaterials, Mater. Today **12**, 34 (2009).
[6] A. L. Cullen, A travelling-wave parametric amplifier, Nature (London) **181**, 332 (1958).

[7] P. K. Tien and H. Suhl, A traveling-wave ferromagnetic amplifier, Proc. IRE **46**, 700 (1958).

[8] E. Cassedy and A. Oliner, Dispersion relations in time-space periodic media: Part I—Stable interactions, Proc. IEEE **51**, 1342 (1963).

[9] E. Cassedy, Dispersion relations in time-space periodic media part II—Unstable interactions, Proc. IEEE **55**, 1154 (1967).

[10] G. Trainiti and M. Ruzzene, Non-reciprocal elastic wave propagation in spatiotemporal periodic structures, New J. Phys. **18**, 083047 (2016).

[11] H. Nassar, X. C. Xu, A. N. Norris, and G. L. Huang, Modulated phononic crystals: Non-reciprocal wave propagation and Willis materials, J. Mech. Phys. Solids **101**, 10 (2017).

[12] H. Nassar, H. Chen, A. N. Norris, M. R. Haberman, and G. L. Huang, Non-reciprocal wave propagation in modulated elastic metamaterials, Proc. R. Soc. A. **473**, 20170188 (2017).

[13] H. Nassar, H. Chen, A. Norris, and G. Huang, Non-reciprocal flexural wave propagation in a modulated metabeam, Extreme Mech. Lett. **15**, 97 (2017).

[14] M. H. Ansari, M. A. Attarzadeh, M. Nouh, and M. A. Karami, Application of magnetoelastic materials in spatiotemporally modulated phononic crystals for nonreciprocal wave propagation, Smart Mater. Struct. **27**, 015030 (2018).

[15] Y. Wang, B. Yousefzadeh, H. Chen, H. Nassar, G. Huang, and C. Daraio, Observation of Nonreciprocal Wave Propagation in a Dynamic Phononic Lattice, Phys. Rev. Lett. **121**, 194301 (2018).

[16] B. M. Goldsberry, S. P. Wallen, and M. R. Haberman, Non-reciprocal wave propagation in mechanically modulated continuous elastic metamaterials, J. Acoust. Soc. Am. **146**, 782 (2019).

[17] Y. Chen, X. Li, H. Nassar, A. N. Norris, C. Daraio, and G. Huang, Nonreciprocal Wave Propagation in a Continuum-Based Metamaterial with Space-Time Modulated Resonators, Phys. Rev. Appl. **11**, 064052 (2019).

[18] X. Zhu, J. Li, C. Shen, X. Peng, A. Song, L. Li, and S. A. Cummer, Non-reciprocal acoustic transmission via space-time modulated membranes, Appl. Phys. Lett. **116**, 034101 (2020).

[19] J. Marconi, E. Riva, M. Di Ronco, G. Cazzulani, F. Braghin, and M. Ruzzene, Experimental Observation of Nonreciprocal Band Gaps in a Space-Time-Modulated Beam Using a Shunted Piezoelectric Array, Phys. Rev. Appl. **13**, 031001(R) (2020).

[20] H. Nassar, B. Yousefzadeh, R. Fleury, M. Ruzzene, A. Alù, C. Daraio, A. N. Norris, G. Huang, and M. R. Haberman, Nonreciprocity in acoustic and elastic materials, Nat. Rev. Mater. **5**, 667 (2020).

[21] J. R. Reyes-Ayona and P. Halevi, Observation of genuine wave vector (k or β) gap in a dynamic transmission line and temporal photonic crystals, Appl. Phys. Lett. **107**, 074101 (2015).

[22] E. Galiffi, P. A. Huidobro, and J. B. Pendry, Broadband Nonreciprocal Amplification in Luminal Metamaterials, Phys. Rev. Lett. **123**, 206101 (2019).

[23] G. Trainiti, Y. Xia, J. Marconi, G. Cazzulani, A. Erturk, and M. Ruzzene, Time-Periodic Stiffness Modulation in Elastic Metamaterials for Selective Wave Filtering: Theory and Experiment, Phys. Rev. Lett. **122**, 124301 (2019).

[24] S. Lee, J. Park, H. Cho, Y. Wang, B. Kim, C. Daraio, and B. Min, Parametric oscillation of electromagnetic waves in momentum band gaps of a spatiotemporal crystal, Photonics Rese. **9**, 142 (2021).

[25] N. Kruss and J. Paulose, Nondispersive One-Way Signal Amplification in Sonic Metamaterials, Phys. Rev. Appl. **17**, 024020 (2022).

[26] D. Torrent, W. J. Parnell, and A. N. Norris, Loss compensation in time-dependent elastic metamaterials, Phys. Rev. B **97**, 014105 (2018).

[27] F. Li, C. Chong, J. Yang, P. G. Kevrekidis, and C. Daraio, Wave transmission in time- and space-variant helicoidal phononic crystals, Phys. Rev. E **90**, 053201 (2014).

[28] E. Fermi, J. Pasta, S. Ulam, and M. Tsingou, Studies of nonlinear problems, Technical Report No. LA-1940 (Los Alamos Scientific Laboratory, 1955), https://www.osti.gov/biblio/4376203.

[29] J. Ford, The Fermi-Pasta-Ulam problem: Paradox turns discovery, Phys. Rep. **213**, 271 (1992).

[30] A. L. Chen and Y.-S. Wang, Study on band gaps of elastic waves propagating in one-dimensional disordered phononic crystals, Phys. B: Condens. Matter **392**, 369 (2007).

[31] N. Boechler, J. Yang, G. Theocharis, P. G. Kevrekidis, and C. Daraio, Tunable vibrational band gaps in one-dimensional diatomic granular crystals with three-particle unit cells, J. Appl. Phys. **109**, 074906 (2011).

[32] G. Gantzounis, M. Serra-Garcia, K. Homma, J. M. Mendoza, and C. Daraio, Granular metamaterials for vibration mitigation, J. Appl. Phys. **114**, 093514 (2013).

[33] N. Boechler, G. Theocharis, and C. Daraio, Bifurcation-based acoustic switching and rectification, Nat. Mater. **10**, 665 (2011).

[34] C. Daraio, V. F. Nesterenko, E. B. Herbold, and S. Jin, Energy Trapping and Shock Disintegration in a Composite Granular Medium, Phys. Rev. Lett. **96**, 058002 (2006).

[35] N. Boechler, G. Theocharis, S. Job, P. G. Kevrekidis, M. A. Porter, and C. Daraio, Discrete Breathers in One-Dimensional Diatomic Granular Crystals, Phys. Rev. Lett. **104**, 244302 (2010).

[36] G. Theocharis, N. Boechler, P. G. Kevrekidis, S. Job, M. A. Porter, and C. Daraio, Intrinsic energy localization through discrete gap breathers in one-dimensional diatomic granular crystals, Phys. Rev. E **82**, 056604 (2010).

[37] M. Toda, Wave propagation in anharmonic lattices, J. Phys. Soc. Jpn. **23**, 501 (1967).

[38] V. F. Nesterenko, Propagation of nonlinear compression pulses in granular media, J. Appl. Mech. Tech. Phys. **24**, 733 (1984).

[39] M. Molerón, A. Leonard, and C. Daraio, Solitary waves in a chain of repelling magnets, J. Appl. Phys. **115**, 184901 (2014).

[40] M. Serra-Garcia, M. Molerón, and C. Daraio, Tunable, synchronized frequency down-conversion in magnetic lattices with defects, Philos. Trans. R. Soc. A **376**, 20170137 (2018).

[41] R. K. Narisetti, M. J. Leamy, and M. Ruzzene, A perturbation approach for predicting wave propagation in one-dimensional nonlinear periodic structures, J. Vibration Acoust. **132**, 031001 (2010).

[42] K. L. Manktelow, M. J. Leamy, and M. Ruzzene, Weakly nonlinear wave interactions in multi-degree of freedom periodic structures, Wave Motion **51**, 886 (2014).

[43] Y.-Z. Wang, F.-M. Li, and Y.-S. Wang, Influences of active control on elastic wave propagation in a weakly nonlinear phononic crystal with a monoatomic lattice chain, Int. J. Mech. Sci. **106**, 357 (2016).

[44] X. Fang, J. Wen, B. Bonello, J. Yin, and D. Yu, Wave propagation in one-dimensional nonlinear acoustic metamaterials, New J. Phys. **19**, 053007 (2017).
[45] P. Kevrekidis, Non-linear waves in lattices: Past, present, future, IMA J. Appl. Math. **76**, 389 (2011).
[46] G. P. Berman and F. M. Izrailev, The Fermi-Pasta-Ulam problem: Fifty years of progress, Chaos **15**, 015104 (2005).
[47] S. Flach and A. Gorbach, Discrete breathers: Advances in theory and applications, Phys. Rep. **467**, 1 (2008).
[48] Y. Starosvetsky, K. R. Jayaprakash, M. A. Hasan, and A. F. Vakakis, *Dynamics and Acoustics of Ordered Granular Media* (World Scientific, Singapore, 2017).
[49] P. G. Kevrekidis, *The Discrete Nonlinear Schrödinger Equation: Mathematical Analysis, Numerical Computations and Physical Perspectives* (Springer, New York, 2009).
[50] C. Chong and P. G. Kevrekidis, *Coherent Structures in Granular Crystals: From Experiment and Modelling to Computation and Mathematical Analysis* (Springer, New York, 2018).
[51] V. Nesterenko, *Dynamics of Heterogeneous Materials* (Springer-Verlag, New York, 2001).
[52] M. Soljačić, M. Ibanescu, S. G. Johnson, Y. Fink, and J. D. Joannopoulos, Optimal bistable switching in nonlinear photonic crystals, Phys. Rev. E **66**, 055601(R) (2002).
[53] F. Y. Wang, G. X. Li, H. L. Tam, K. W. Cheah, and S. N. Zhu, Optical bistability and multistability in one-dimensional periodic metal-dielectric photonic crystal, Appl. Phys. Lett. **92**, 211109 (2008).
[54] C.-P. Wen, W. Liu, and J.-W. Wu, Tunable terahertz optical bistability and multistability in photonic metamaterial multilayers containing nonlinear dielectric slab and graphene sheet, Appl. Phys. A **126**, 426 (2020).
[55] D. A. Powell, I. V. Shadrivov, and Y. S. Kivshar, Multistability in nonlinear left-handed transmission lines, Appl. Phys. Lett. **92**, 264104 (2008).
[56] A. B. Kozyrev, H. Kim, and D. W. van der Weide, Parametric amplification in left-handed transmission line media, Appl. Phys. Lett. **88**, 264101 (2006).
[57] D. A. Powell, I. V. Shadrivov, and Y. S. Kivshar, Asymmetric parametric amplification in nonlinear left-handed transmission lines, Appl. Phys. Lett. **94**, 084105 (2009).
[58] S. Mukherjee and M. C. Rechtsman, Observation of Unidirectional Solitonlike Edge States in Nonlinear Floquet Topological Insulators, Phys. Rev. X **11**, 041057 (2021).
[59] S. P. Wallen and M. R. Haberman, Nonreciprocal wave phenomena in spring-mass chains with effective stiffness modulation induced by geometric nonlinearity, Phys. Rev. E **99**, 013001 (2019).
[60] J. Vila, R. K. Pal, M. Ruzzene, and G. Trainiti, A Bloch-based procedure for dispersion analysis of lattices with periodic time-varying properties, J. Sound Vib. **406**, 363 (2017).
[61] J. A. Richards, Stability diagram approximation for the lossy Mathieu equation, SIAM J. Appl. Math. **30**, 240 (1976).
[62] W.-C. Xie, *Dynamic Stability of Structures* (Cambridge University Press, Cambridge, 2006).
[63] C. S. Huang, S. L. Hung, W. C. Su, and C. L. Wu, Identification of time-variant modal parameters using time-varying autoregressive with exogenous input and low-order polynomial function, Comput.-Aided Civil Infrastruct. Eng. **24**, 470 (2009).
[64] I. Kovacic, R. Rand, and S. M. Sah, Mathieu's equation and its generalizations: Overview of stability charts and their features, Appl. Mech. Rev. **70**, 020802 (2018).
[65] J. N. Kutz, Advanced differential equations: Asymptotics & perturbations, arXiv:2012.14591 (2020).
[66] A. H. Nayfeh and D. T. Mook, *Nonlinear Oscillations* (Wiley and Sons, Weinheim, 2004).
[67] E. Doedel and L. S. Tuckerman, *Numerical Methods for Bifurcation Problems and Large-Scale Dynamical Systems* (Springer-Verlag, Heidelberg, 2000).
[68] M. Sato, B. E. Hubbard, and A. J. Sievers, Colloquium: Nonlinear energy localization and its manipulation in micromechanical oscillator arrays, Rev. Mod. Phys. **78**, 137 (2006).
[69] C. Chong, P. G. Kevrekidis, G. Theocharis, and C. Daraio, Dark breathers in granular crystals, Phys. Rev. E **87**, 042202 (2013).